



A genetic mammalian proportional–integral feedback control circuit for robust and precise gene regulation

Timothy Frei^{a,1}, Ching-Hsiang Chang^{a,1}, Maurice Filo^a, Asterios Arampatzis^a, and Mustafa Khammash^{a,2}

Edited by Jens Nielsen, BioInnovation Institute, DK2200 Copenhagen, Denmark; received December 10, 2021; accepted April 13, 2022

The processes that keep a cell alive are constantly challenged by unpredictable changes in its environment. Cells manage to counteract these changes by employing sophisticated regulatory strategies that maintain a steady internal milieu. Recently, the antithetic integral feedback motif has been demonstrated to be a minimal and universal biological regulatory strategy that can guarantee robust perfect adaptation for noisy gene regulatory networks in *Escherichia coli*. Here, we present a realization of the antithetic integral feedback motif in a synthetic gene circuit in mammalian cells. We show that the motif robustly maintains the expression of a synthetic transcription factor at tunable levels even when it is perturbed by increased degradation or its interaction network structure is perturbed by a negative feedback loop with an RNA-binding protein. We further demonstrate an improved regulatory strategy by augmenting the antithetic integral motif with additional negative feedback to realize antithetic proportional–integral control. We show that this motif produces robust perfect adaptation while also reducing the variance of the regulated synthetic transcription factor. We demonstrate that the integral and proportional–integral feedback motifs can mitigate the impact of gene expression burden, and we computationally explore their use in cell therapy. We believe that the engineering of precise and robust perfect adaptation will enable substantial advances in industrial biotechnology and cell-based therapeutics.

synthetic gene circuits | proportional–integral feedback | robust perfect adaptation | variance reduction

The ability to maintain a steady internal environment in the presence of a changing and uncertain external environment—called homeostasis—is a defining characteristic of living systems (1). Homeostasis is maintained by various regulatory mechanisms, often in the form of negative feedback loops. The importance of homeostasis is clearly exemplified in physiology and medicine, where a loss of homeostasis is often attributed to the development of disease (2–4).

Feedback control systems in engineering use the error, or, more specifically, the difference between the desired output—commonly referred to as the setpoint—and the current output of the system which is to be regulated, to determine the effort that the control system applies to steer the system under control. In a simple proportional feedback system, the effort is determined by the instantaneous difference. Therefore, if the difference becomes zero when the desired output is reached, no effort is applied, and the output is free to deviate from the desired state. Compared to this simpler proportional feedback, integral feedback does not just feed back the instantaneous difference between the desired state and the current state but uses the entire history of the difference to determine the control effort applied (Fig. 1D). This difference may build up and will provide control effort even as the error has decayed to zero. It can be shown that this strategy can guarantee that a zero difference between desired output and current output is achieved in the steady-state, leading to perfect adaptation (5). Indeed, the output of a system with integral feedback is known to perfectly adapt to constant disturbances in the parameters and structure of the system under control and is also able to perfectly track a desired constant input signal, commonly referred to as the setpoint. More recently, it has become increasingly evident that integral feedback is a regulatory strategy that drives biological adaptation in different systems (6–10). Although integral feedback guarantees robust perfect adaptation, it does not, in general, prevent large transient deviations. To mediate this, control engineers often augment proportional feedback to their integral feedback control systems. By counteracting such large deviations, proportional–integral (PI) feedback also suppresses large stochastic fluctuations around the setpoint and therefore provides more precise regulation than integral feedback can achieve (11).

Here, we demonstrate perfect adaptation in a sense/antisense messenger RNA (mRNA) implementation of the antithetic integral feedback circuit in mammalian cells and show that the resulting closed-loop control system is highly robust to network changes and parameter disturbances. By further incorporating proportional feedback on the sensed output to achieve PI feedback control, we also increase the precision of the resulting

Significance

To survive in the harsh environments they inhabit, cells have evolved sophisticated regulatory mechanisms that can maintain a steady internal milieu or homeostasis. This robustness, however, does not generally translate to engineered genetic circuits, such as the ones studied by synthetic biology. Here, we introduce an implementation of a minimal and universal gene regulatory motif that produces robust perfect adaptation for mammalian cells, and we improve on it by enhancing the precision of its regulation.

Author affiliations: ^aDepartment of Biosystems Science and Engineering, Eidgenössische Technische Hochschule (ETH) Zürich, 4058 Basel, Switzerland

Author contributions: T.F., C.-H.C., M.F., and M.K. designed research; T.F., C.-H.C., M.F., A.A. and M.K. performed research; T.F. and C.-H.C. contributed new reagents/analytic tools; T.F., C.-H.C., and M.F. analyzed data; T.F., C.-H.C., M.F., A.A., and M.K. wrote the paper; T.F. and C.-H.C. performed experiments; M.F. performed mathematical modeling and data fitting; and M.K. supervised research and secured funding.

The authors declare a competing interest. ETH Zürich has filed a patent application on behalf of the inventors T.F., C.-H.C., M.F., and M.K. on the genetic circuit designs described (application no. EP20206417.6).

This article is a PNAS Direct Submission.

Copyright © 2022 the Author(s). Published by PNAS. This open access article is distributed under [Creative Commons Attribution-NonCommercial-NoDerivatives License 4.0 \(CC BY-NC-ND\)](https://creativecommons.org/licenses/by-nc-nd/4.0/).

¹T.F. and C.-H.C. contributed equally to this work.

²To whom correspondence may be addressed. Email: mustafa.khammash@bsse.ethz.ch.

This article contains supporting information online at <https://www.pnas.org/lookup/suppl/doi:10.1073/pnas.2122132119/-DCSupplemental>.

Published June 10, 2022.

adaptation. Furthermore, we derive a mathematical (mechanistic) model that describes the various interactions in the system. We show that the obtained model fits the experimentally obtained data well, and is also capable of predicting the robustness features of our implementation of the antithetic integral controller. Lastly, we demonstrate the applicability of our integral and PI controllers by demonstrating perfect mitigation of the gene expression burden and show that the PI controller provides superior precision over integral feedback.

Over the last decade, several experimental studies have constructed RNA-based genetic control systems (12–14) to regulate gene expression, and have constructed cell-based therapies that implement negative feedback loops to mitigate disease (15–18). These, however, rely solely on proportional feedback rather than integral or PI feedback and are therefore not guaranteed to achieve precise and robust regulation. In 2016, Briat et al. (19) introduced a biomolecular circuit topology that implements integral feedback control for general biomolecular systems. Fig. 1*A* depicts an abstract representation of this control motif. A subsequent publication by the same authors (11) showed that additional proportional negative feedback further reduces variance in the controlled output. Central to this strategy—termed antithetic PI feedback—is the so-called annihilation (or sequestration) reaction between the two species that implement the controller (reaction with rate η in Fig. 1*A*). The annihilation refers to the requirement that both controller species abolish each other's function when they interact. Another stringent requirement to achieve integral feedback is that the two controller species on their own remain fairly stable over time. Given these conditions, any network interconnected in a stable way with this antithetic integral controller will achieve robust adaptation (Fig. 1*C*). The incorporation of additional proportional negative feedback from the output of the controlled network to the actuation reaction then yields PI feedback (Fig. 1*A*). Independent of integral feedback, this proportional feedback introduces a reduction in the variance of the controlled output (Fig. 1*C*).

The initial theoretical work has motivated the implementation of antithetic integral control in bacteria (20, 21) and in vitro (22). A quasi-integral controller in *Escherichia coli* (23) also relies on a similar topology. In realizing antithetic integral feedback, one of the main challenges is identifying a suitable implementation of the annihilation (or sequestration) reaction (21). In the bacterial implementation of the antithetic integral feedback motif (21), stable proteins (a σ and anti- σ factor pair) were used to realize the sequestration reaction. However, this approach is not directly applicable to mammalian cells. Instead, in this work, we exploit hybridization of complementary mRNAs to realize this critical reaction (Fig. 2*A*). For the antithetic integral controller to function properly, the sense and antisense RNAs have to be stable such that their degradation is predominantly due to their mutual interaction (via the hybridization reaction). Unlike bacterial RNAs where the majority of mRNAs have half-lives between 3 and 8 min (24), mammalian RNAs are much more stable, with typical mRNA half-lives of several hours (25). Indeed, in human cells, the majority of mRNAs have half-lives between 6 and 18 h, with an overall mean value of 10 h (26, 27). The hybridization of the mammalian sense/antisense RNAs and their stability allow us to realize the antithetic integral controller in mammalian cells. Sense and antisense mRNA have previously been employed to control gene expression in yeast (28) and to build a genetic oscillator in mammalian cells (29). Furthermore, antisense RNA has shown promise in the treatment of cancer and other genetic diseases as well as infections (30–32).

Results

Integral Feedback. A schematic depiction of the sense/antisense RNA implementation of the antithetic integral feedback circuit is shown in Fig. 2*A*. The basic circuit consists of two genes, which are encoded on separate plasmids. The gene in the activator plasmid is the synthetic transcription factor tTA (tetracycline transactivator) (33) fused to the fluorescent protein mCitrine. The expression of this gene is driven by the strong mammalian EF-1 α promoter. This transcription factor drives the expression of the other gene in the antisense plasmid via the tTA-responsive TRE promoter. This gene expresses an antisense RNA that is complementary to the activator mRNA. The hybridization of these two species realizes the annihilation (or sequestration) reaction and closes the negative feedback loop. Note that the successful realization of the antithetic integral controller hinges on the suitable choice of the sequestration pair participating in the sequestration reaction. For instance, we show, in *SI Appendix, section E*, via analytic reasoning and numerical simulations, that, if the sequestration reaction is reversible and/or it produces an active complex that inherits the functionality of one of the two sequestered molecules, then the adaptation property is lost. These undesirable features are virtually nonexistent with the sense/antisense sequestration pair, rendering them as good candidates to realize the antithetic integral controller. As an experimental control incapable of producing integral feedback, we built an open-loop analog of the closed-loop circuit, in which the TRE promoter was replaced by a noncognate promoter. The closed-loop configuration is set up to regulate the expression levels of the activator tTA-mCitrine. To introduce specific perturbations to the activator, we additionally fused an Asunaprevir (ASV) inducible degradation tag (SMASh) to tTA-mCitrine (34).

To show that our genetic implementation of the circuit performs integral feedback, we apply constant disturbances with ASV at a concentration of 0.033 μM to HEK293T cells which were transiently transfected with either the open- or the closed-loop circuit. Additionally, we vary the setpoint by transfecting the two plasmids at ratios ranging from 1/16 to 2 (activator plasmid/ntisense plasmid). The fluorescence of the cells was measured 48 h after transfection, using flow cytometry. As the setpoint ratio increases, so does the fluorescence of tTA-mCitrine, indicating that our circuit permits setpoint control (Fig. 2*B* and *SI Appendix, Fig. S8*). Even for low setpoint ratios, the fluorescence remained above background levels (*SI Appendix, Fig. S14*). Note that this fluorescence is a monotonically increasing function of the plasmid ratios (see also the function θ in *SI Appendix, Fig. S1B*). We consider a circuit to be adapting if its normalized fluorescence intensity stays within 10% of the undisturbed control. Under this criterion, adaptation is achieved for all the setpoints tested below two in the closed-loop configuration. In contrast, none of the open-loop configurations manage to meet this adaptation requirement (Fig. 2*C*).

Next, we sought to demonstrate that our implementation of the antithetic integral controller will provide disturbance rejection at different setpoints regardless of the network topology it regulates. Therefore, we added a negative feedback loop from tTA-mCitrine to its own production. This negative feedback was realized by the RNA-binding protein L7Ae (35), which is expressed under the control of a tTA-responsive TRE promoter and binds the kink-turn hairpin on the sense mRNA to inhibit translation (Fig. 2*A*). The closed- and open-loop circuits were transiently transfected either with or without this negative feedback plasmid to introduce a perturbation to the regulated network. The setpoints 1/4 and 1/2 were tested by transfecting an appropriate ratio of the

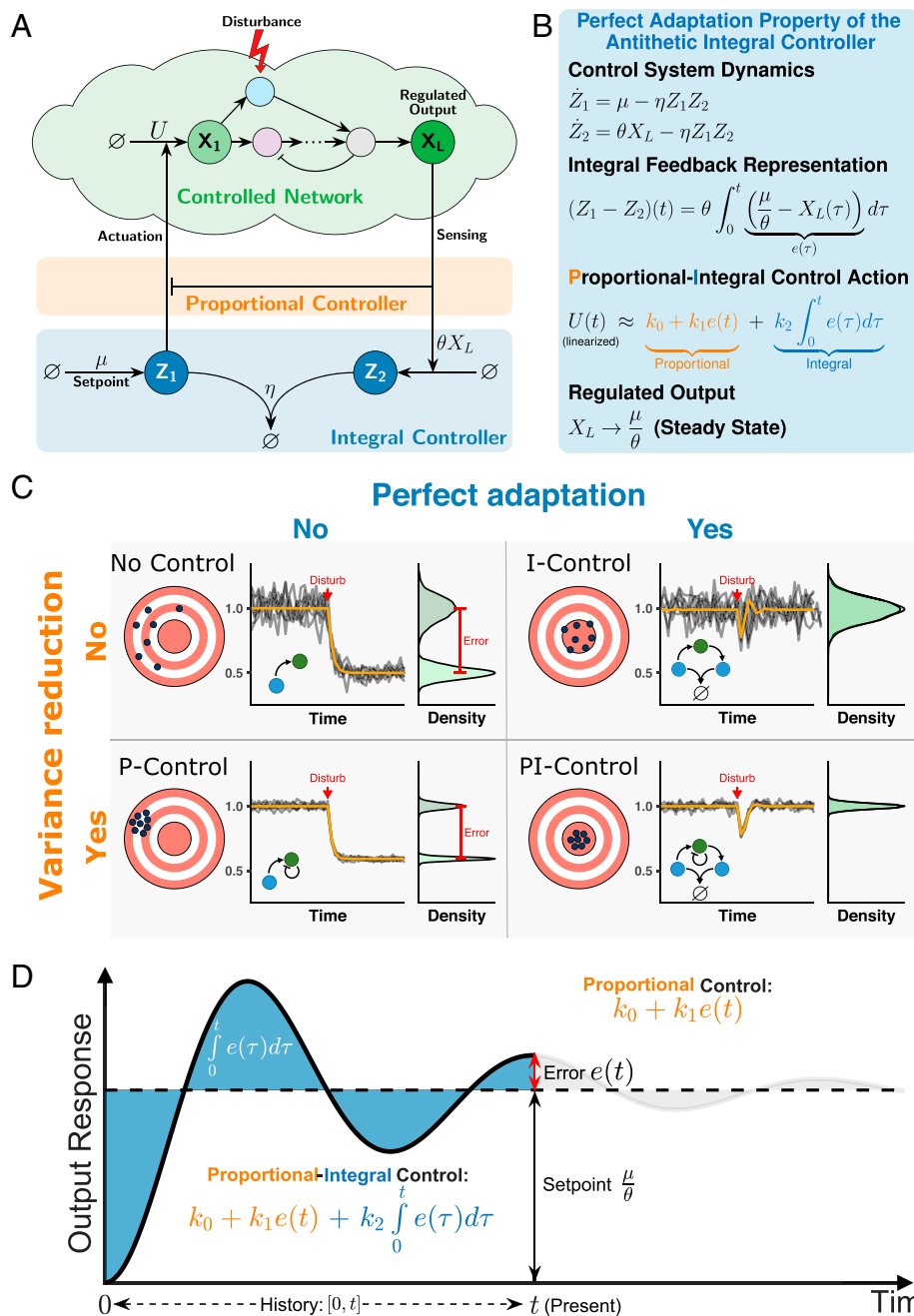


Fig. 1. The antithetic PI feedback motif. (A) Network topology of an arbitrary molecular network interacting with an antithetic PI feedback motif. The nodes labeled with Z_1 and Z_2 together compose the antithetic motif responsible for realizing integral feedback. Species Z_1 is produced at a rate μ and is functionally annihilated when it interacts with species Z_2 at a rate η . Furthermore, Z_1 interacts with the controlled network by promoting the production of species X_1 . To close the feedback loop, species Z_2 is produced at a reaction rate that is proportional to θ and the regulated output species X_L . An additional negative feedback from the output to the production reaction extends the motif to PI feedback. (B) Dynamics of the antithetic integral controller. Subtracting the differential equations of Z_1 and Z_2 reveals the integral action of the controller that ensures that the steady state of the output converges to a value that is independent of the controlled network parameters. Additionally, through linearization (36), the individual integral and the proportional control actions of the antithetic PI motif can be expressed separately. (C) The elements of PI feedback. Without any feedback control, the output of the controlled network may be highly variable and will likely respond drastically to a disturbance in the network. By adding integral feedback, it can be assured that the output will adapt perfectly to disturbances. Conversely, by adding proportional feedback, the variability in the output can be reduced. Combining the two types of feedback reduces the variability of the output while also ensuring perfect adaptation. (D) Graphical demonstration of integral and proportional control. Integral control accounts for error history by mathematically integrating it in time. Consequently, integral controllers have memory and “remember” the past. However, proportional controllers act instantaneously by only accounting for the present error. Consequently, proportional controllers are memoryless and “forget” the past.

activator to antisense plasmids. These different conditions were further perturbed at the molecular level by adding $0.033 \mu\text{M}$ of ASV to induce degradation of tTA-mCitrine. As shown in Fig. 2D (see also *SI Appendix, Fig. S2, Left*), the closed-loop circuit rejects both perturbations nearly perfectly in all cases, whereas, again, the open-loop circuit fails to adapt.

PI Feedback. The capability of the antithetic integral controller to reject topological network perturbations, as demonstrated previously in Fig. 2D, allowed us to further improve the controller performance by increasing its complexity. In particular, we implement a common control strategy that is extensively applied in various engineering disciplines, referred to as PI control. This

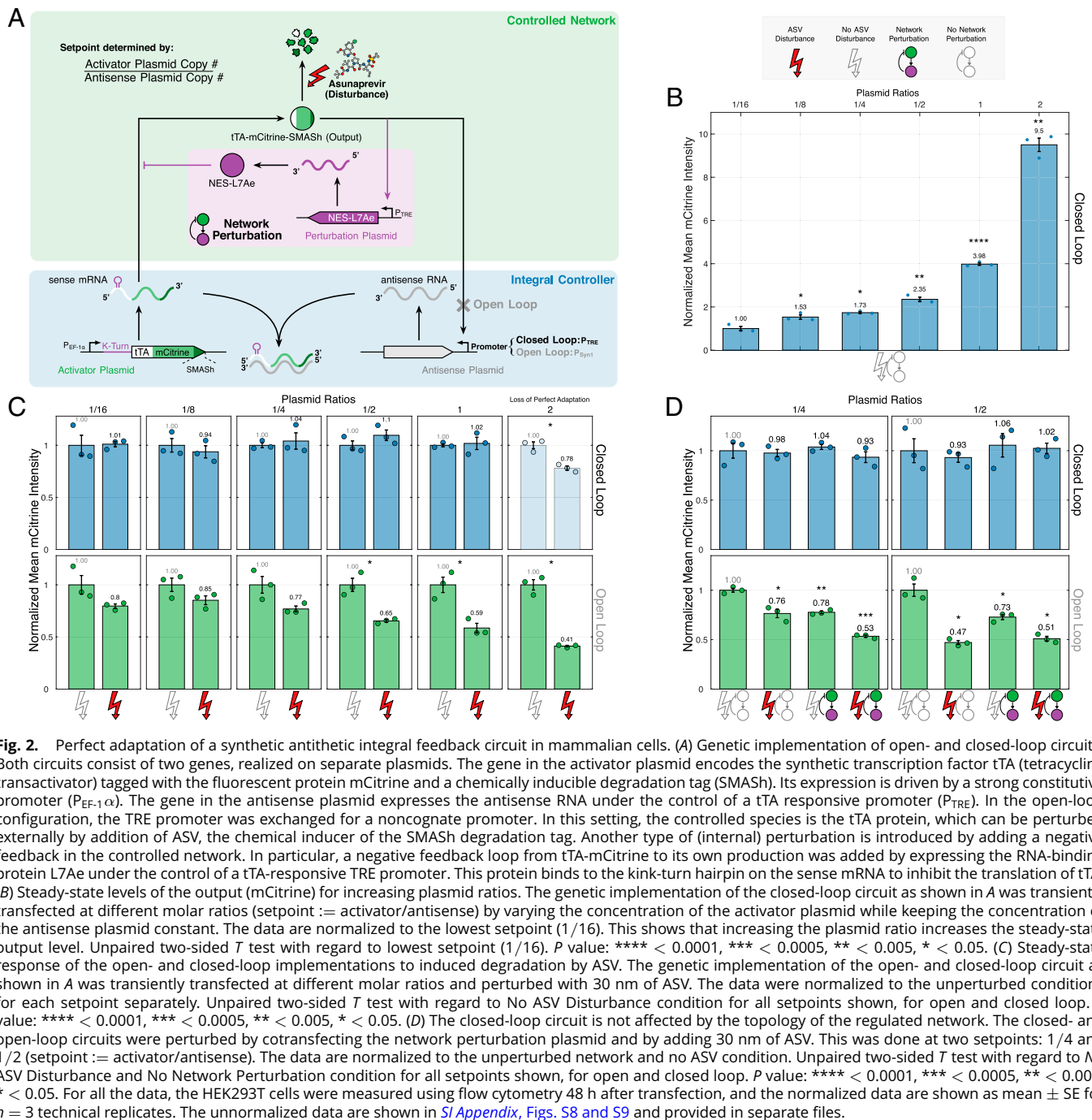


Fig. 2. Perfect adaptation of a synthetic antithetic integral feedback circuit in mammalian cells. (A) Genetic implementation of open- and closed-loop circuits. Both circuits consist of two genes, realized on separate plasmids. The gene in the activator plasmid encodes the synthetic transcription factor tTA (tetracycline transactivator) tagged with the fluorescent protein mCitrine and a chemically inducible degradation tag (SMASH). Its expression is driven by a strong constitutive promoter ($P_{EF-1\alpha}$). The gene in the antisense plasmid expresses the antisense RNA under the control of a tTA responsive promoter (P_{TRE}). In the open-loop configuration, the TRE promoter was exchanged for a noncognate promoter. In this setting, the controlled species is the tTA protein, which can be perturbed externally by addition of ASV, the chemical inducer of the SMASH degradation tag. Another type of (internal) perturbation is introduced by adding a negative feedback in the controlled network. In particular, a negative feedback loop from tTA-mCitrine to its own production was added by expressing the RNA-binding protein L7Ae under the control of a tTA-responsive TRE promoter. This protein binds to the kink-turn hairpin on the sense mRNA to inhibit the translation of tTA. (B) Steady-state levels of the output (mCitrine) for increasing plasmid ratios. The genetic implementation of the closed-loop circuit as shown in A was transiently transfected at different molar ratios (setpoint := activator/antisense) by varying the concentration of the activator plasmid while keeping the concentration of the antisense plasmid constant. The data are normalized to the lowest setpoint (1/16). This shows that increasing the plasmid ratio increases the steady-state output level. Unpaired two-sided T test with regard to lowest setpoint (1/16). P value: **** < 0.0001 , *** < 0.0005 , ** < 0.005 , * < 0.05 . (C) Steady-state response of the open- and closed-loop implementations to induced degradation by ASV. The genetic implementation of the open- and closed-loop circuit as shown in A was transiently transfected at different molar ratios and perturbed with 30 nM of ASV. The data were normalized to the unperturbed conditions for each setpoint separately. Unpaired two-sided T test with regard to No ASV Disturbance condition for all setpoints shown, for open and closed loop. P value: **** < 0.0001 , *** < 0.0005 , ** < 0.005 , * < 0.05 . (D) The closed-loop circuit is not affected by the topology of the regulated network. The closed- and open-loop circuits were perturbed by cotransfecting the network perturbation plasmid and by adding 30 nM of ASV. This was done at two setpoints: 1/4 and 1/2 (setpoint := activator/antisense). The data are normalized to the unperturbed network and no ASV condition. Unpaired two-sided T test with regard to No ASV Disturbance and No Network Perturbation condition for all setpoints shown, for open and closed loop. P value: **** < 0.0001 , *** < 0.0005 , ** < 0.005 , * < 0.05 . For all the data, the HEK293T cells were measured using flow cytometry 48 h after transfection, and the normalized data are shown as mean \pm SE for $n = 3$ technical replicates. The unnormalized data are shown in [SI Appendix, Figs. S8 and S9](#) and provided in separate files.

control strategy adds to the integral (I) controller proportional (P) feedback action to enhance dynamic performance, such as transient dynamics and variance reduction (11, 36, 37), while maintaining the adaptation property. To implement proportional feedback control that acts faster than the integral feedback, we use a proxy protein, namely, the RNA-binding protein L7Ae, which is produced in parallel with mCitrine-tTA from a single mRNA via the use of a P2A self-cleavage peptide (Fig. 3A). Therefore, the expression level of L7Ae is expected to proportionally reflect the level of tTA-mCitrine. The negative feedback is hence realized via the proxy protein that inhibits translation by binding the 5' untranslated region of the sense mRNA. Note that, as opposed to the circuit in Fig. 2A, the production of L7Ae in the PI controller is not regulated by the tTA responsive TRE promoter. Instead, it is directly controlled by the sense mRNA. Furthermore,

the proportional feedback realized in the PI controller is expected to act faster than the feedback implemented by the tTA-dependent production of L7Ae (Fig. 2A), because it does not require additional transcription and translation steps. Refer to [SI Appendix, section D](#) for a detailed mathematical analysis, using linear perturbation theory, that reveals the underlying PI structure of the controller.

As illustrated in Fig. 3B, with a standalone proportional controller, increasing the proportional feedback strength via introducing additional L7Ae-binding hairpins has the effect of reducing the steady-state error induced by the drug disturbance. Nonetheless, despite the error reduction, our criteria of adaptation is not met. On the other hand, with a PI controller, the expression of tTA-mCitrine is ensured to be robust to the induced drug disturbance as depicted in Fig. 3. This demonstrates that the

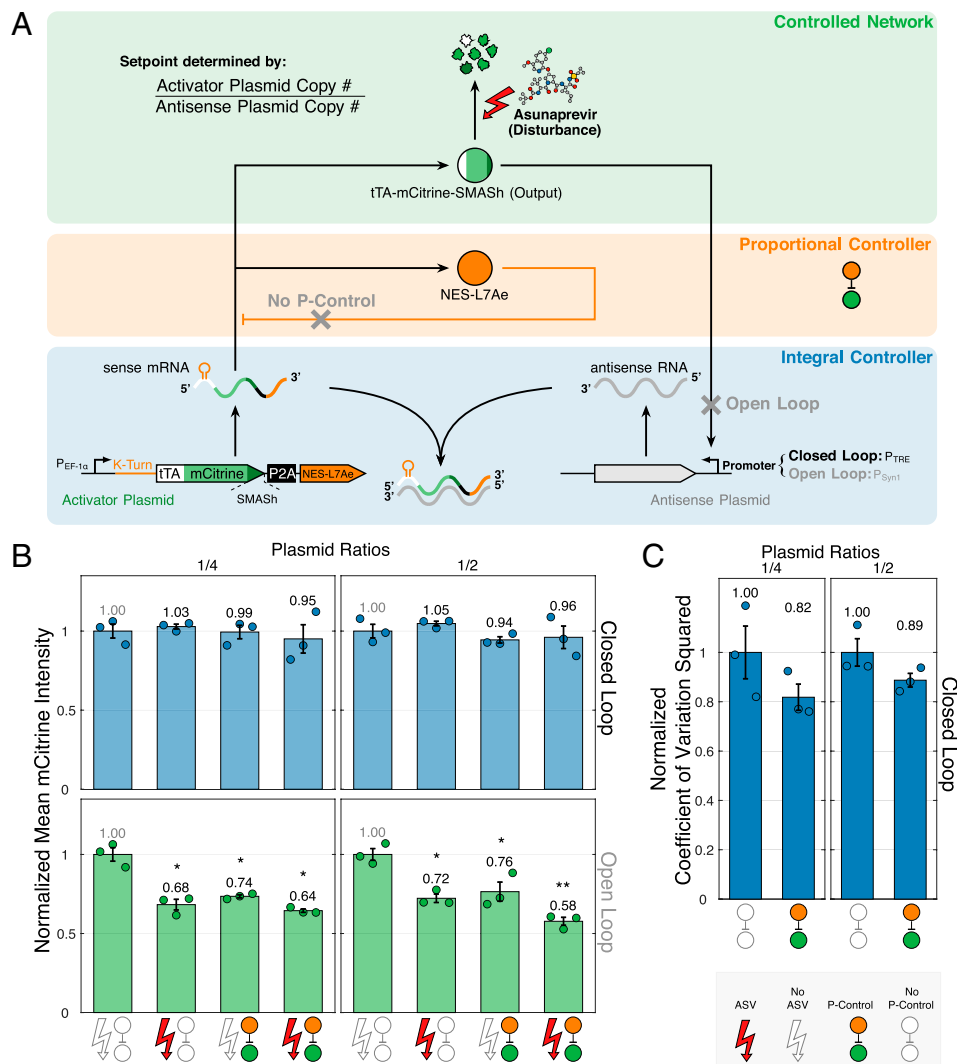


Fig. 3. A PI controller. (A) Genetic implementation of a PI controller. A negative feedback loop from the RNA-binding protein L7Ae (which is proxy to tTA-mCitrine since it is simultaneously produced from the same mRNA) is added to the antithetic motif. This protein binds in the 5' untranslated region of the sense mRNA species to inhibit the translation of tTA and itself simultaneously. Stronger proportional feedback is realized by adding additional L7Ae-binding hairpins. (B) A PI controller does not break the adaptation property. The P and PI circuits were implemented by adding a negative feedback loop from L7Ae to the open- and closed-loop circuits. All circuits were perturbed by adding 30 nM of ASV. The HEK293T cells were measured using flow cytometry 48 h after transfection, and the data are shown as mean per condition normalized to the unperturbed (no ASV) condition \pm SE for $n = 3$ technical replicates. Unpaired two-sided T test with regard to No ASV and No P-Control condition for all setpoints shown, for open and closed loops. P value: ** < 0.005 , * < 0.05 . (C) PI control reduces the steady-state variance. Computing the normalized coefficient of variation squared on the steady-state flow cytometry distributions reveals a reduction in variation in the presence of proportional feedback. The coefficients of variation squared were normalized to the No P-Control condition for both setpoints and are shown \pm SE for $n = 3$ technical replicates. Unpaired two-sided T test with regard to No P-Control condition for all setpoints shown. The unnormalized data are shown in *SI Appendix, Figs. S10 and S11* and provided in a separate file.

additional proportional feedback indeed does not break the adaptation property of the antithetic integral controller, as predicted by control theory.

Mathematical Modeling. To demonstrate that the circuits in Figs. 2A and 3A are consistent with our understanding of the regulatory topologies, we first derive detailed mechanistic models of these topologies, starting from basic principles of mass-action kinetics. Next, a model reduction technique is carried out based on a quasi-steady-state approximation that exploits the timescale separation imposed by the various fast binding/unbinding reactions in the network. The mathematical details can be found in *SI Appendix, sections A–C*, where each circuit is mathematically treated separately. The resulting reduced models are all compactly presented in a single reaction network depicted in Fig. 4A. The overall network can be divided into two biomolecular controller subnetworks—the integral and proportional controllers—that are connected in feedback with another subnetwork to be

controlled. This is illustrated schematically in Fig. 4A and mathematically as a set of ordinary differential equations in *SI Appendix, Figs. S1B, S3B, and S4B*. The reduced models capture the expression dynamics of the three genes, denoted by G_1 , G_2 , and G'_2 , that are encoded in the activator, antisense, and network perturbation plasmids, respectively. Gene G_1 is constitutively expressed at a rate $\mu(G_1)$, while the other two genes, G_2 and G'_2 , are activated by the (dimer) transcription factor A at rates $\theta(A; G_2)$ and $\theta_p(A; G'_2)$, respectively. The derived mathematical expressions of the functions μ , θ , θ_p and the active degradation propensity, λ , are all given in *SI Appendix, Figs. S1B and S4B*. Note that the model for the circuit of Fig. 2A without (with) network perturbation can be obtained by setting $G'_2 = \tau = 0$ ($\tau = 0$), whereas, the model for the circuit of Fig. 3A can be obtained by setting $G'_2 = 0$ and $\tau = 1$.

Next, we calibrate the derived mathematical models to the experimental measurements that were collected at steady state. The measured fluorescence, denoted by M , represents all the

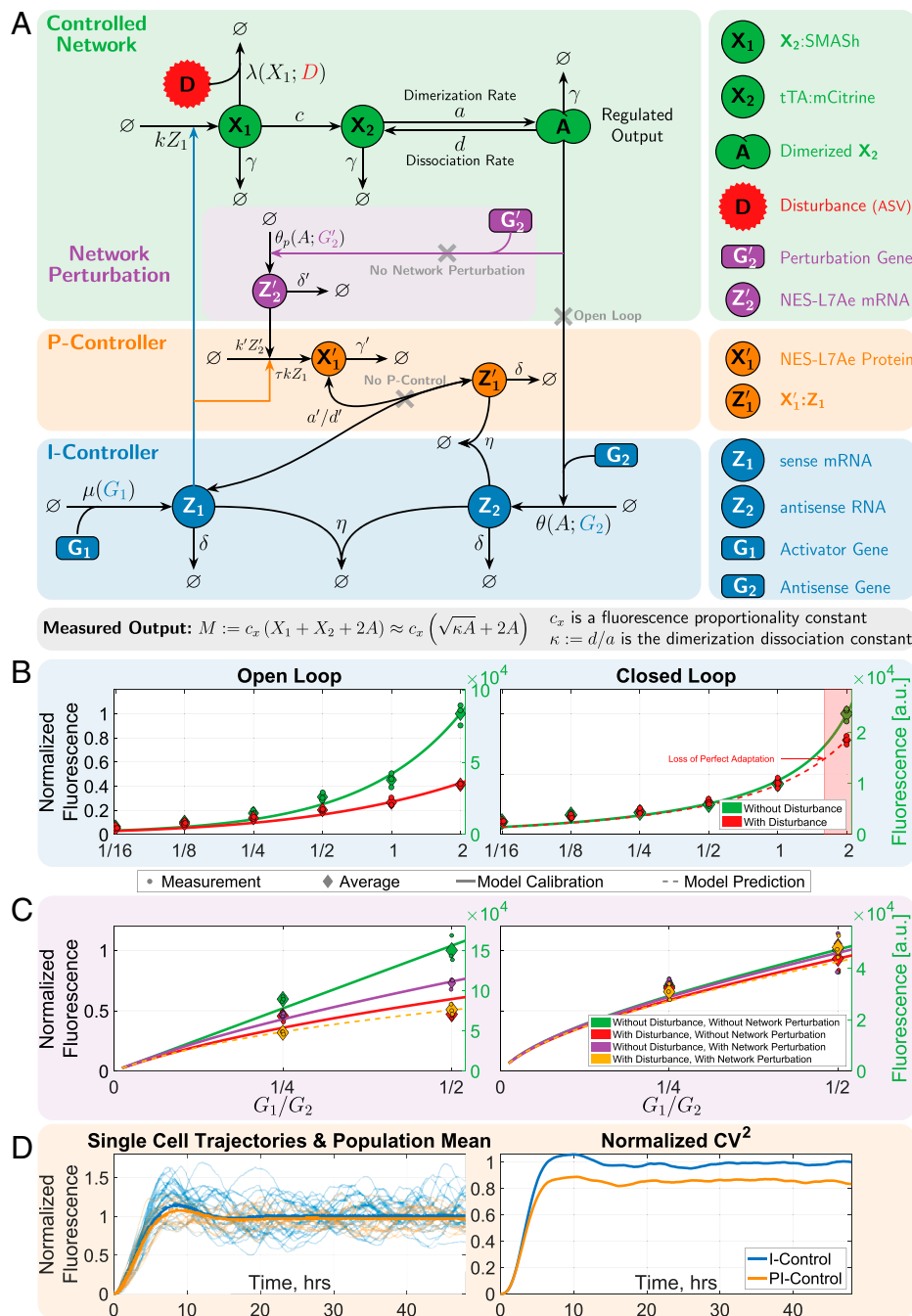


Fig. 4. Mathematical modeling of the various circuits. (A) A chemical reaction network compactly modeling the various circuits presented in Figs. 2 and 3. The sense mRNA, Z_1 , is constitutively produced at a rate $\mu(G_1)$ that depends on the gene (plasmid) concentration, G_1 . Then, Z_1 is translated into a fusion of a synthetic transcription factor, fluorescent protein, and inducible-degradation tag, referred to as X_1 , at a rate k . X_1 is either actively degraded by the ASV disturbance D at a rate $\lambda(X_1; D)$ or converted to X_2 at a rate c by releasing the SMASH tag. The protein X_2 dimerizes to form A , which activates the transcription of the antisense RNA, Z_2 . The transcription rate, denoted by θ , is a function of A and the gene concentration G_2 . The antithetic integral control, shown in the blue box, is modeled by the sequestration of Z_1 and Z_2 at a rate η . Note that the open-loop circuit is obtained by removing the feedback from the regulated output A . The proportional controller (orange box) is modeled by producing the protein X'_1 , also at a rate k , in parallel with X_1 to serve as its proxy. A negative feedback is then achieved by the (un)binding reaction between the proxy X'_1 and Z_1 . Finally, the network perturbation (purple box) is modeled by introducing an additional gene G'_2 . This gene is activated by A to transcribe the mRNA Z'_2 at a rate θ_p which is a function of A and G'_2 . Z'_2 is then translated into the protein X'_1 that has, once again, a negative feedback on the production of X_1 by binding to Z_1 . See *SI Appendix, Figs. S1, S3, and S4* for a detailed mathematical explanation for each separate circuit. (B and C) Model calibrations to experimental data. (Left) The model fits for the open-loop circuits with/without disturbance (B) and with/without network perturbation (C). (Right) Similarly, the model fits for the closed-loop circuits. The model fits for proportional control are reported in *SI Appendix, Fig. S4C*. The solid lines denote model fits, while dashed lines denote model predictions. The model fits and predictions show a very good agreement with the experiments over a wide range of plasmid ratios (setpoints) G_1/G_2 , for all scenarios. (D) Stochastic simulations demonstrating the variance reduction property of the proportional controller. The calibrated steady-state parameter groups of the PI closed-loop circuit, given in *SI Appendix, Eq. S42*, are fixed, while the time-related parameters are set as follows: $\gamma = \gamma', k = c = d = 1 \text{ min}^{-1}$ to demonstrate the variance reduction property that is achieved when a proportional controller is appended to the antithetic integral motif. Note that $G_1 = 0.002 \text{ pmol}$, and $G_2 = 0.004 \text{ pmol}$.

molecules involving mCitrine: X_1 , X_2 , and A . It is shown in *SI Appendix, section A.4* that M can be expressed solely in terms of the concentration of the regulated output A , as shown

at the bottom of Fig. 4A, where c_x is an instrument-related proportionality constant that maps concentrations in nanometers to fluorescence in arbitrary units, and κ is the dimerization

dissociation constant of **A**. Of course, steady-state measurements alone cannot uniquely estimate all parameters in the model. However, by carrying out a steady-state analysis of the underlying differential equations, we can identify a set of parameter groups (or aggregated parameters) that can be uniquely estimated based on the collected data. The detailed mathematical analyses, showing the aggregated parameter groups and their calibrated values, are reported for each circuit separately in *SI Appendix, sections A.5, B.3, and C.3*.

In the ideal closed-loop scenario where the dilution/degradation rate δ is zero, the steady-state analyses are fairly straightforward and are shown at the bottom of *SI Appendix, Figs. S1B, S3B, and S4B* for each circuit. These analyses show that the steady-state concentration of the regulated output, denoted by \bar{A} , is the same for all the circuits and is given by

$$\bar{A} = \kappa_2 \frac{r - k_0/k_2}{1 - r}, \quad \text{with} \quad r := \frac{k_1 G_1}{k_2 G_2}. \quad [1]$$

Observe that \bar{A} is a monotonically increasing function of the plasmid ratio G_1/G_2 , and is independent of the various controlled network parameters, particularly the disturbance D and the plasmid concentration G'_2 . As a result, robust perfect adaptation is exactly achieved, since the ASV disturbance and the network perturbation have absolutely no effect on the steady-state concentration of the regulated output **A**.

In practice, the dilution/degradation rate δ is never exactly zero, which makes the integrator “leaky.” In this case, the steady-state analysis becomes more involved, and one cannot obtain an explicit formula for \bar{A} as in the ideal situation. However, implicit (polynomial) formulae can be obtained and are used here to fit the mathematical models to the data. It should be pointed out that, when δ is sufficiently small relative to other controller rate parameters (as can be achieved with slowly growing cells and fairly stable sense/antisense RNA), the integrator leakiness will be negligibly small, and perfect adaptation can still be achieved for all practical purposes (21, 38). This is verified experimentally in Figs. 2 *C* and *D* and 3*B*. The model fits for the integral circuit of Fig. 2*A*, shown in Fig. 4*B*, are carried out sequentially for the open-loop circuit first (with and without disturbance), and then for the closed-loop circuit (without disturbance). This sequential procedure avoids overfitting the model to the data. Finally, the closed-loop circuit with disturbance was left for model prediction to assess the calibration accuracy. As shown in the plots of Fig. 4*B*, the model fits the data very well, and is also capable of predicting the experimentally observed disturbance rejection feature of the antithetic integral controller (dashed red curve in Fig. 4*B, Right*). Similar model calibration procedures were also carried out for the circuits of *SI Appendix, Figs. S3A and S4A*, and the model fits and predictions are reported in Fig. 4*C* and *SI Appendix, Fig. S4C*, respectively. Clearly, the models fit the data quite well, and are also capable of predicting another experimentally observed feature of the antithetic integral controller: robustness to network perturbations. The models also show that appending the proportional controller to the integral controller does not affect the steady state of the measured output, but it is capable of reducing the stationary variance (equivalently, the coefficient of variation), as demonstrated experimentally in Fig. 3*C* (*SI Appendix, Fig. S11B*) and theoretically through the stochastic simulations depicted in Fig. 4*D*.

Gene Expression Burden Mitigation. To demonstrate the antithetic integral and PI controllers in a more practical setting, we apply the circuits introduced in Figs. 2 and 3 to decouple the expression of the transcription factor tTA-mCitrine-SMASH from

the expression of other genes when they are competing for finite pools of shared resources. This effect was first described in bacteria (39) and, later, also characterized in mammalian cells (40, 41). The effective consequence of this is that changes in the expression of one gene inversely affect the expression of all other genes that share a pool of resources with it. In the context of feedback control, the aforementioned changes in gene expression can be seen as disturbances to the controlled network (Fig. 5*A*). To experimentally introduce this perturbation, we cotransfected varying amounts of an additional disturbance plasmid that constitutively expresses the fluorescent protein mRFP670. Previously, it had been observed that the expression of transiently transfected genes is repressed by the presence of double-stranded RNA (dsRNA) (42). We similarly observed that the dsRNA formed through the hybridization of sense and antisense mRNA inhibits the expression of the additionally transfected mRFP670 (comparing Closed Loop to Syn1 Open Loop in *SI Appendix, Fig. S12*). To make the gene expression burden—reflected by mRFP670 expression levels—comparable between the closed-loop and open-loop conditions, we replaced the inactive Syn1 promoter with a constitutively active EF1 α promoter and tuned the plasmid ratio such that the expression of mRFP670 matches the closed-loop expression (Low EF1 α Antisense condition in *SI Appendix, Fig. S12*). As was already done in Fig. 3, we now compare the responses of the open-loop (No Control), proportional feedback (P-Control), integral feedback (I-Control), and PI (PI-Control) variants to this new disturbance. As can be seen in Fig. 5*B* (*SI Appendix, Fig. S13A*), a setpoint of 1/2 is maintained within 10% up to a disturbance strength of 2.3 for I-Control and for all disturbance strengths for PI-Control (Fig. 5*B* and *SI Appendix, Fig. S13A*). This is not the case for the No Control and P-Control configurations, where the steady-state error steadily increases with the increasing strength of the disturbance (Fig. 5*B* and *SI Appendix, Fig. S13A*). In all cases, the disturbance is similar in relative extent (Fig. 5 *B, Top* and *SI Appendix, Fig. S13 A, Top*). In addition to providing perfect adaptation, PI-Control improves regulation over I-Control by further reducing the steady-state cell-to-cell variability (Fig. 5*C* and *SI Appendix, Fig. S13B*).

Discussion and Application Prospects

This study presents an implementation of integral and PI feedback in mammalian cells. With our proof-of-principle circuit, we lay the foundation for robust and predictable control systems engineering in mammalian biology. We believe PI feedback systems will have a transformative effect on the field of synthetic biology, just like they have had on other engineering disciplines.

Based on the antithetic motif (Fig. 1*A*), we designed and built a proof-of-concept circuit capable of perfect adaptation. This was achieved by exploiting the hybridization of mRNA molecules to complementary antisense RNAs. The resulting inhibition of translation realized the central sequestration mechanism. Specifically, we expressed an antisense RNA through a promoter that was activated by the transcription factor tTA. This antisense RNA was complementary to and bound with the mRNA of tTA to close the negative feedback loop (Fig. 2*A*). We further highlighted the properties of integral feedback control by showing that our circuit permits different setpoints. By applying a disturbance to the regulated species, we showed that the closed-loop circuit achieved adaptation and provided superior robustness compared to an analogous open-loop circuit (Fig. 2*C*). Further, we showed that adaptation was also achieved when the setpoint of the circuit was changed. Note that the setpoint of the antithetic integral controller is determined by the ratio between sense and antisense

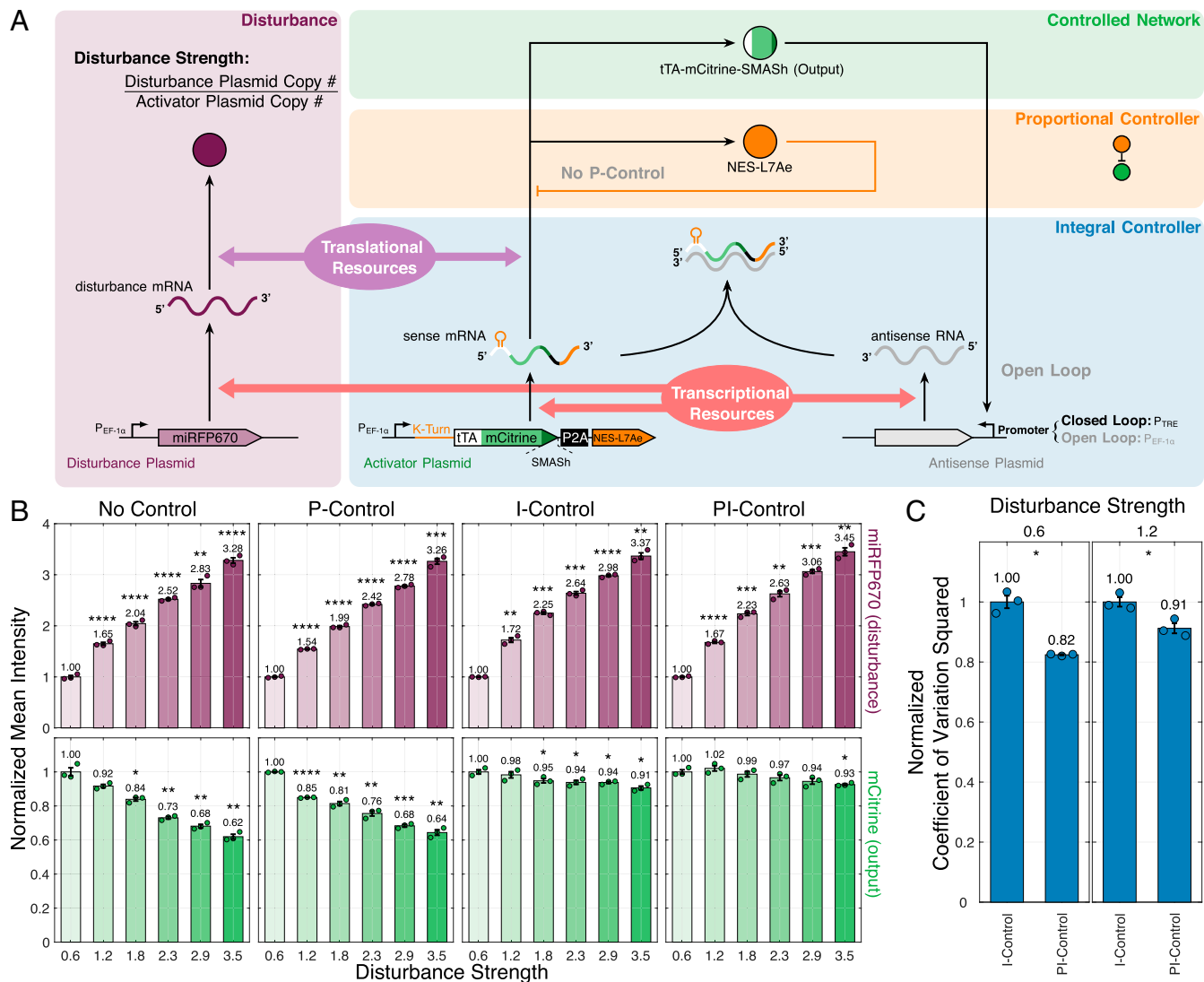


Fig. 5. Mitigating competition for shared limited resources with antithetic integral and PI feedback. (A) A genetic implementation of an antithetic integral and PI feedback circuit for mitigating the effects of limited shared resources. The antithetic integral and PI feedback circuit characterized in Figs. 2 and 3 are repurposed to mitigate the coupling of gene expression induced by shared pools of finite resources. Varying the amounts of an additional disturbance plasmid that constitutively expresses the fluorescent protein mRFP670 introduces a disturbance to the amount of available resources, which indirectly affects the expression levels of tTA-mCitrine-SMASH. (B) Steady-state rejection of disturbances to available limited shared resources. The activator plasmid and antisense plasmid for all conditions were transiently transfected at a setpoint ratio of 1/2 together with disturbance strengths varying from 0.6 to 3.5. The *Top* and *Bottom* rows, respectively, show the fluorescence of the mRFP670 disturbance and mCitrine output normalized to the lowest disturbance strength. The disturbance strength describes the amount of disturbance plasmid relative to the activator plasmid. Unpaired two-sided *T* test with regard to lowest disturbance strength (0.6) for all controllers, for open and closed loop. *P* value: **** < 0.0001 , *** < 0.0005 , ** < 0.005 , * < 0.05 . (C) Reduction in cell-to-cell variability as a result of PI feedback control. The coefficient of variation squared was computed for the first two disturbance strengths and normalized to the lowest disturbance strength. Unpaired two-sided *T* test with regard to I-Control for both setpoints shown. *P* value: **** < 0.0001 , *** < 0.0005 , ** < 0.005 , * < 0.05 . The data are shown as the mean \pm SE for $n = 3$ technical replicates per condition. The unnormalized data are shown in *SI Appendix, Fig. S13* and provided in a separate file.

mRNA plasmid. Although plasmids might dilute during cell division, both plasmids are distributed randomly without bias to the daughter cells. Therefore, the average ratio of the two plasmids should remain the same after division. An earlier implementation of the antithetic integral feedback motif in bacteria (21) used a σ and anti- σ factor pair to realize the sequestration reaction. Due to the requirement of factors native to the bacterial cell for σ factors to activate transcription, this approach is not directly applicable to mammalian cells. Conversely, the sense and antisense RNA approach utilized in this study is likely to be more difficult to realize in bacterial cells, due to rapid mRNA turnover.

Moreover, we demonstrated that our realization of the antithetic integral feedback motif is agnostic to the network structure of the regulated species. This was achieved by introducing a perturbation to the controlled network itself (Fig. 2D and

SI Appendix, Fig. S9). Furthermore, we also demonstrated that the closed-loop circuit still rejected disturbances, even in the presence of this extra perturbation to the network. In the open-loop circuit, the disturbance, perturbation, and perturbation with disturbance all led to a strong decrease in tTA-mCitrine expression.

Next, we used the perturbation to the controlled network to incorporate proportional feedback into our integral control circuit directly. We then showed that this PI feedback controller maintained the same setpoint as the integral controller, even when challenged with induced degradation of the controlled species. To demonstrate that this new controller did utilize proportional feedback, we showed a reduction in the cell-to-cell variability by computing the coefficient of variation squared on the measured fluorescence distributions.

To test our understanding of the mechanistic interactions within our circuits, we derived mechanistic mathematical models for the circuits, starting from basic mass-action kinetics, and showed that the obtained models were capable of fitting the experimental measurements. We also showed that the models were capable of predicting key features of our implementation of the antithetic PI controller: disturbance rejection and robustness to network perturbations.

Finally, we employed our integral and antithetic integral feedback circuits to perfectly mitigate gene expression burden on the controlled species caused by introducing an additional, constructively expressed fluorescent protein at varying levels. In light of recent studies on the effects of shared cellular resources in mammalian cells (40, 41), it is important to point out that the dependence of the production of the two controller species on the same resource pool (e.g., transcriptional resources for sense/antisense RNAs) was crucial for maintaining the setpoint despite variations in resource availability. This derives from the fact that the setpoint is a function of the ratio of the production rates of the two controller species (ratio r in Eq. 1). Whenever both rates depend similarly on the same resource pool, the effect of this dependence cancels out. When the production rates depend on different resource pools, they do not cancel out, and the setpoint becomes sensitive to resource allocation.

In previous work describing the effects of shared cellular resources in mammalian cells (40, 41), incoherent feedforward (iFF) loop topologies were used to mitigate the indirect coupling of gene expression. Here, we have achieved the same using our antithetic integral and PI feedback circuits. While iFF loops can adapt to inputs [even perfectly in some instances (43, 44)], they typically do so for a single input. In contrast, integral feedback loops can adapt to perturbations in the entire controlled network (43–45).

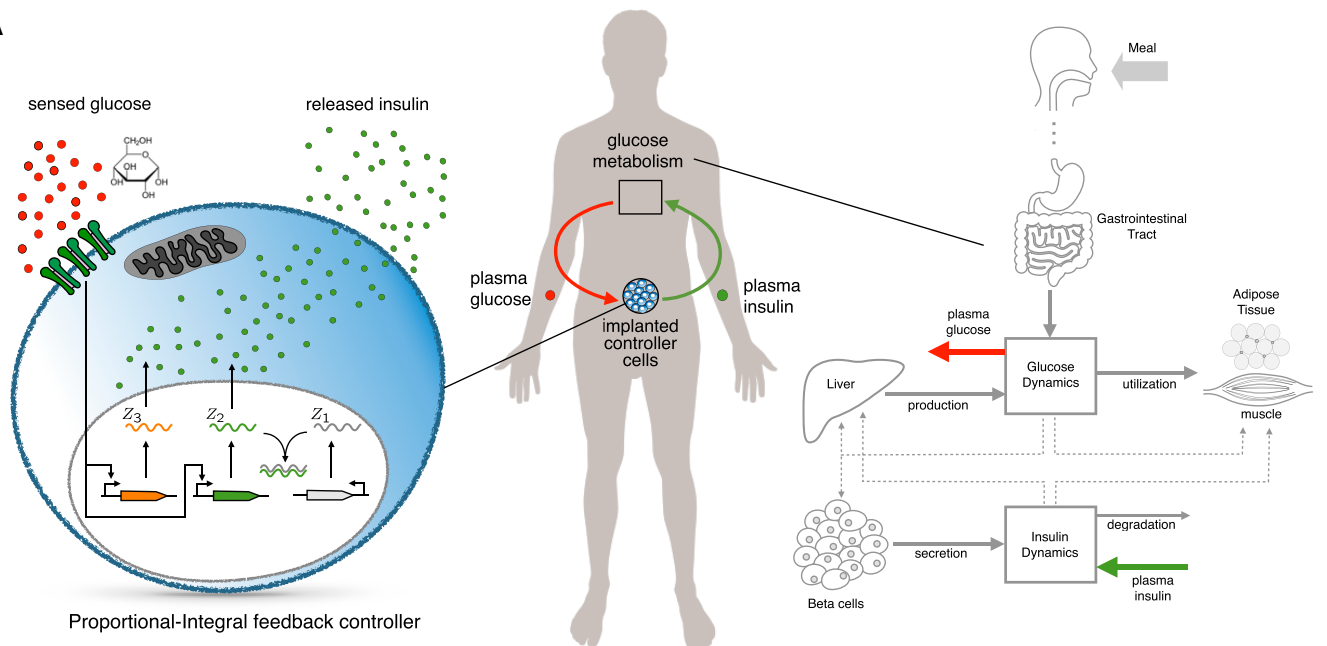
Aside from realizing integral feedback control, the sense and antisense RNA implementation is very simple to adapt and is versatile. Indeed, both sense and antisense are fully programmable, with the only requirement being that they share sufficient sequence homology to hybridize and inhibit translation. Due to this fact, mRNAs of endogenous transcription factors may easily be converted into the antithetic motif simply by expressing their antisense RNA from a promoter activated by the transcription factor. However, one should note that, to successfully implement an antithetic integral feedback controller for a transcription factor of interest, there are several points to consider. 1) The sense and antisense mRNA need to be stable to prevent leaky integration. 2) A suitable promoter that responds monotonically to the desired range of the transcription factor is required to avoid promoter saturation and loss of regulation. 3) Although the setpoint to the transcription factor will be lower than without the antisense RNA due to the negative feedback, the setpoint of the antithetic integral feedback controller can be tuned by increasing the strength of the promoter expressing the sense mRNA, increasing the ratio between the sense/antisense transcription units or decreasing the strength/sensitivity of the promoter expressing the antisense RNA.

In the following, we speculate about prospective applications of the antithetic PI controller for achieving robust and precise regulation of the glucose response in modeled diabetic patients. Genetically engineered controllers have desirable properties as treatment strategies for homeostasis-related pathologies. Previously, it has been demonstrated that, when encapsulated insulin-producing designer cells were implanted in diabetic mice, they alleviated the effects of type 1 diabetes mellitus (T1DM) by secreting insulin in response to low blood pH mediated by diabetic ketoacidosis (46) or, alternatively, in response to sensed glucose (18). This

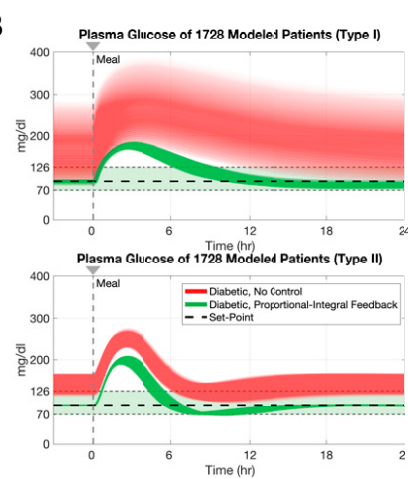
pioneering work provided a proof of concept for the practical feasibility of this approach. In this previous work, however, the designed feedback controller is similar to a standalone proportional controller, and therefore cannot exhibit the property of robust perfect adaptation that is characteristic of integral feedback. We next exploit our antithetic PI controller implementation to carry out a simulation study that demonstrates the achievable robust precision and accuracy of the glucose response in modeled diabetic patients. To illustrate the clinical translatability of our proposed controller topologies, we employed disease models for diabetes mellitus (DM) and interfaced them with the different controller circuits (Fig. 6). The ability of pancreatic β -cells to synthesize and release insulin determines the classification of DM into two main categories: type 1 DM of autoimmune etiology and type 2 DM (T2DM). As a result, we utilized mathematical models for both T1DM (47, 48) and T2DM (49), which originated from the UVA/PADOVA (University of Virginia/Universita di Padova) Type 1 Diabetes Simulator (S2008) and its updated versions (47, 50). This simulator constitutes the first computer model approved by the Food and Drug Administration as an alternative to preclinical trials and animal testing.

Over the past few decades, the prevalence of DM has increased exponentially, and DM is now considered the most common endocrine disease, affecting ~ 1 in 11 adults globally (51). Our results propose a closed-loop alternative to open-loop replacement therapy with exogenous insulin, which, in the case of T1DM, is prescribed for life. They also offer a potentially more manageable approach to the combination of lifestyle changes and pharmacological interventions that is recommended for addressing T2DM management (52). Moreover, we showed that the simulated glucose control is robust to interpatient variability (Fig. 6*B*), for example, due to differences in endogenous glucose production by the liver [clinically found under stress conditions or in critically ill patients (53)], or to changes in renal function, such as physiological or pathological (e.g., diuretic administration, chronic kidney disease) variations in glomerular filtration rate. It was also shown, in Fig. 6*C*, that the antithetic integral and PI controllers were capable of achieving robust adaptation. In contrast, a standalone proportional controller did not meet the desired setpoint, nor could it reject disturbances such as an increase in endogenous glucose production rate (k_{p1} in ref. 49). Note that dissimilarities in the response of the healthy patient and that of the PI controller–treated patient are, for the most part, not due to any differences between the two regulation strategies (natural vs. synthetic). Rather, they are mostly attributed to the fact that, for the treated patient, the insulin was modeled to be synthesized de novo from a genetically engineered synthetic insulin gene, leading to inevitable gene expression delay. In comparison, for healthy patients, insulin is stored in vesicles for quick release, which ensures a more rapid response—a fact that was also accounted for in the model of the healthy patient. Nevertheless, the response of the PI controller–treated patient in Fig. 6*C* meets all the preprandial and peak postprandial plasma glucose guidelines of the American Diabetes Association (54), and hence offers a potentially effective treatment strategy. Interestingly, the same controller for the single T1DM patient of Fig. 6*C*, *Left* was capable of meeting the guidelines for all 1,728 patients in Fig. 6*B*, *Top* without requiring retuning for different patients—a clear demonstration of robust adaptation. A similar robust adaptation was seen in T2DM, where a single controller met the guidelines for the majority of patients. For those patients for whom the guidelines were not met, the violation was slight (glucose levels exceeded 180 mg/dl (milligram per deciliter) only briefly beyond the maximum of 2 h; Fig. 6*B*, *Bottom*). This, however, can be remedied by slightly

A



B



C

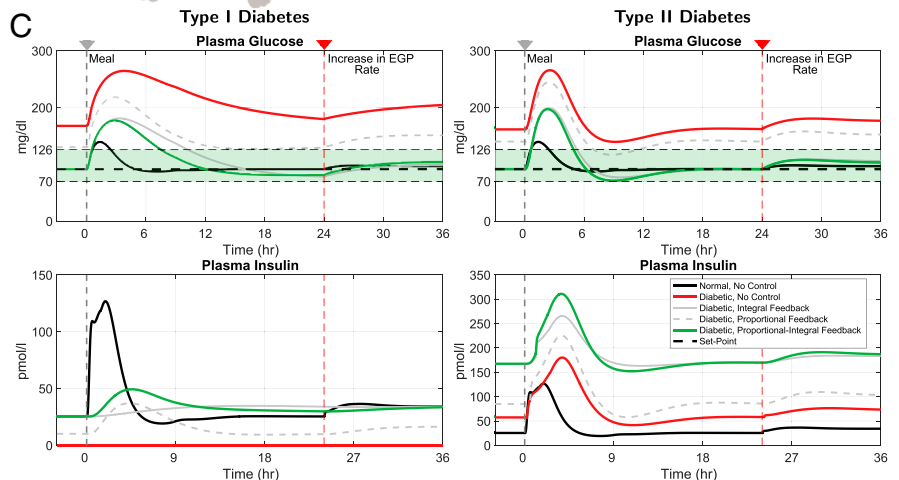


Fig. 6. Simulation of glucose regulation in the blood with antithetic PI control. (A) A schematic representation describing the mathematical model of the closed-loop network. The diagram to the right provides a high-level description of the modeled glucose and insulin dynamics based on ref. 49. This diagram represents the controlled network, where the output of interest (to be controlled) is the glucose concentration (milligrams per dL) in the plasma; whereas, the input that actuates this network is the insulin concentration (picomoles per liter) in the plasma. Note that, unlike the controlled network in the previous figures, this network has a negative gain: Increasing the input (insulin) decreases the output (glucose). Hence, to ensure an overall negative feedback, a P-type controller (with positive gain) is adopted here and shown in the schematic to the left, which models a genetically embedded antithetic PI controller. The P-type property of the integrator is achieved by switching **Z1** with **Z2**; that is, the antisense RNA is now constitutively produced while the sense mRNA “senses” the output (glucose) and actuates the input (insulin). The P-type property of the proportional controller is achieved by using an activation reaction (instead of an inhibition reaction as in Fig. 3A) where glucose activates a gene (in orange) to produce insulin. (B) Robustness to interpatient variability. To demonstrate the robustness of our PI controllers, three parameters $k_{p1} \in [2.4, 3]$, $V_{mx} \in [0.024, 0.071]$, and $k_{e1} \in [0.0003, 0.0008]$ (see ref. 49) in the controlled network are varied, while the controller parameters are fixed. Changes of k_{p1} depict alterations in endogenous glucose production [e.g., in various catabolic or stress states (53)], and V_{mx} is used to simulate variations in the insulin-dependent glucose utilization (U_{id} in ref. 49) in the peripheral tissues (e.g., by physiological or pathological changes in GLUT4 translocation), while k_{e1} is the glomerular filtration rate. The responses are shown for a meal of 40 g of glucose at $t = 0$ and a disturbance in endogenous glucose production (EGP) rate at $t = 24$ h. A single meal comprising 40 g of glucose and an increase of endogenous glucose production rate from $k_{p1} = 2.7$ mg/min \rightarrow 3 mg/min (see ref. 49) is applied to the models of healthy and diabetic subjects at $t = 0$ h and $t = 24$ h, respectively. *Top (Bottom)* depicts the response of glucose (insulin) concentration, whereas *Left (Right)* plots correspond to a type I (type II) diabetic subject. The black curves correspond to a healthy subject whose glucose levels quickly return back to the glycemic target range (for adults with diabetes) [80, 130] mg/dl (54) after the meal, due to naturally secreted insulin. In contrast, the red curves correspond to uncontrolled diabetic patients whose glucose levels are incapable of returning back to the healthy range, due to lack of insulin (type I) or low insulin sensitivity (type II). Finally, the solid gray, dashed gray, and green curves correspond to diabetic patients whose glucose levels are controlled by our integral, proportional, and PI controllers, respectively. Both integral and PI controllers are capable of restoring a healthy level of glucose concentration by tuning the setpoint to a desired value (100 mg/dL), whereas the proportional controller alone is capable of neither returning to the desired setpoint nor rejecting the disturbance. Furthermore, the PI controller outperforms the standalone integral controller by speeding up the convergence to the setpoint, especially for type I diabetes.

retuning the controller for these patients if necessary. The details of the mathematical modeling can be found in [SI Appendix, section F](#).

We believe that the ability to precisely and robustly regulate gene expression in mammalian cells will find many applications

in industrial biotechnology and biomedicine. In the area of biomedicine, these robust, perfectly adapting controllers can be used to restore homeostasis in the treatment of metabolic diseases, as well as for applications in immunotherapy and precise drug delivery.

Materials and Methods

Plasmid Construction. Plasmids for transfection were constructed using a mammalian adaptation of the modular cloning (MoClo) yeast toolkit standard (55). Custom parts for the toolkit were generated by PCR amplification (Phusion Flash High-Fidelity PCR Master Mix; Thermo Scientific) and assembled into toolkit vectors via golden gate assembly (56). All enzymes used for applying the MoClo procedure were obtained from New England Biolabs.

Cell Culture. HEK293T cells (ATCC, strain number CRL-3216) were cultured in Dulbecco's modified Eagle's medium (Gibco) supplemented with 10% fetal bovine serum (Sigma-Aldrich), $1 \times$ GlutaMAX (Gibco), and 1 mM sodium pyruvate (Gibco). The cells were maintained at 37°C and 5% CO_2 . Every 2 d to 3 d, the cells were passaged into a fresh T25 flask. When required, surplus cells were plated for transfection.

Transfection. Cells used in transfection experiments were plated in a 96-well plate at 10,000 to 15,000 cells per well or in a 24-well plate at 70,000 to 80,000 cells per well ~ 24 h before treatment with the transfection solution. Alternatively, for the experiments shown in Fig. 5, the cell suspension diluted to $\sim 140,000$ to 160,000 cells per well was used to quench the transfection solution directly. The 24-well plates were then seeded from the resulting solution. The transfection solution was prepared using polyethylenimine (PEI) "MAX" (MW 40000; Polysciences, Inc.) at a 1:3 (micrograms of DNA to micrograms of PEI) ratio with a total of 100 ng of plasmid DNA for the 96-well plate or 500 ng of plasmid DNA for the 24-well plate. The specific amounts of plasmid and cells used for

each experiment are summarized in *SI Appendix, Tables S10–S15*. All plasmids used for transfection are summarized in *SI Appendix, Table S16*. The solution was prepared in Opti-MEM I (Gibco) and incubated for ~ 25 min prior to addition to the cells.

Flow Cytometry. Approximately 48 h after transfection, the cells were collected in $60\ \mu\text{L}$ of Accutase solution (Sigma-Aldrich). The fluorescence was measured on a Beckman Coulter CytoFLEX S flow cytometer using the 488-nm laser with a 525/40+OD1 band-pass filter. For each sample, the whole cell suspension was collected. In each measurement, additional unstained and single-color (mCitrine only) controls were collected for gating and compensation.

Data Analysis. The acquired data were analyzed using a custom analysis pipeline implemented in the R programming language. The measured events are automatically gated and compensated for further plotting and analysis.

Data Availability. All study data are included in GitLab (<https://gitlab.ethz.ch/freitim/a-genetic-mammalian-proportional-integral-feedback-control-circuit-for-robust-and-precise-gene-regulation>) and/or *SI Appendix*.

ACKNOWLEDGMENTS. We thank Dr. Gabriele Lillacci and Eline Bijman for their support during the early stage of the project. We also thank Drs. Stephanie Aoki and Ankit Gupta for reading the manuscript and providing many useful comments. M.K. acknowledges funding from the European Research Council under the European Union's Horizon 2020 research and innovation program (CyberGenetics; Grant Agreement 743269).

1. L. A. Urry, M. L. Cain, S. A. Wasserman, P. V. Minorsky, J. B. Reece, *Campbell Biology* (Pearson Education, Incorporated, 2017).
2. M. E. Kotas, R. Medzhitov, Homeostasis, inflammation, and disease susceptibility. *Cell* **160**, 816–827 (2015).
3. R. Mullur, Y. Y. Liu, G. A. Brent, Thyroid hormone regulation of metabolism. *Physiol. Rev.* **94**, 355–382 (2014).
4. F. X. Yu, B. Zhao, K. L. Guan, Hippo pathway in organ size control, tissue homeostasis, and cancer. *Cell* **163**, 811–828 (2015).
5. K. J. Åström, R. M. Murray, *Feedback Systems: An Introduction for Scientists and Engineers* (Princeton University Press, 2010).
6. T. M. Yi, Y. Huang, M. I. Simon, J. Doyle, Robust perfect adaptation in bacterial chemotaxis through integral feedback control. *Proc. Natl. Acad. Sci. U.S.A.* **97**, 4649–4653 (2000).
7. H. El-Samad, J. P. Goff, M. Khammash, Calcium homeostasis and parturient hypocalcemia: An integral feedback perspective. *J. Theor. Biol.* **214**, 17–29 (2002).
8. P. Miller, X. J. Wang, Inhibitory control by an integral feedback signal in prefrontal cortex: A model of discrimination between sequential stimuli. *Proc. Natl. Acad. Sci. U.S.A.* **103**, 201–206 (2006).
9. D. Muzey, C. A. Gómez-Urbe, J. T. Mettetal, A. van Oudenaarden, A systems-level analysis of perfect adaptation in yeast osmoregulation. *Cell* **138**, 160–171 (2009).
10. D. Ben-Zvi, N. Barkai, Scaling of morphogen gradients by an expansion-repression integral feedback control. *Proc. Natl. Acad. Sci. U.S.A.* **107**, 6924–6929 (2010).
11. C. Briat, A. Gupta, M. Khammash, Antithetic proportional-integral feedback for reduced variance and improved control performance of stochastic reaction networks. *J. R. Soc. Interface* **15**, 20180079 (2018).
12. J. A. Stapleton *et al.*, Feedback control of protein expression in mammalian cells by tunable synthetic translational inhibition. *ACS Synth. Biol.* **1**, 83–88 (2012).
13. R. J. Bloom, S. M. Winkler, C. D. Smolke, Synthetic feedback control using an RNAi-based gene-regulatory device. *J. Biol. Eng.* **9**, 5 (2015).
14. G. Lillacci, Y. Benenson, M. Khammash, Synthetic control systems for high performance gene expression in mammalian cells. *Nucleic Acids Res.* **46**, 9855–9863 (2018).
15. C. Kemmer *et al.*, Self-sufficient control of urate homeostasis in mice by a synthetic circuit. *Nat. Biotechnol.* **28**, 355–360 (2010).
16. P. Wei *et al.*, Bacterial virulence proteins as tools to rewire kinase pathways in yeast and immune cells. *Nature* **488**, 384–388 (2012).
17. K. Rössger, G. Charpin-El-Hamri, M. Fussenegger, A closed-loop synthetic gene circuit for the treatment of diet-induced obesity in mice. *Nat. Commun.* **4**, 2825 (2013).
18. M. Xie *et al.*, β -cell-mimetic designer cells provide closed-loop glycemic control. *Science* **354**, 1296–1301 (2016).
19. C. Briat, A. Gupta, M. Khammash, Antithetic integral feedback ensures robust perfect adaptation in noisy biomolecular networks. *Cell Syst.* **2**, 15–26 (2016).
20. G. Lillacci, S. Aoki, D. Schweingruber, M. Khammash, A synthetic integral feedback controller for robust tunable regulation in bacteria. *Biorxiv* [Preprint] (2017). <https://doi.org/10.1101/170951> (Accessed 22 March 2022).
21. S. K. Aoki *et al.*, A universal biomolecular integral feedback controller for robust perfect adaptation. *Nature* **570**, 533–537 (2019).
22. D. K. Agrawal, R. Marshall, V. Noireaux, E. D. Sontag, In vitro implementation of robust gene regulation in a synthetic biomolecular integral controller. *Nat. Commun.* **10**, 5760 (2019).
23. H. H. Huang, Y. Qian, D. Del Vecchio, A quasi-integral controller for adaptation of genetic modules to variable ribosome demand. *Nat. Commun.* **9**, 5415 (2018).
24. R. Milo, R. Phillips, *Cell Biology by the Numbers* (Garland Science, 2015).
25. J. E. Pérez-Ortín, P. Alepuz, S. Chávez, M. Choder, Eukaryotic mRNA decay: Methodologies, pathways, and links to other stages of gene expression. *J. Mol. Biol.* **425**, 3750–3775 (2013).
26. E. Yang *et al.*, Decay rates of human mRNAs: Correlation with functional characteristics and sequence attributes. *Genome Res.* **13**, 1863–1872 (2003).
27. B. Schwanhäusser *et al.*, Global quantification of mammalian gene expression control. *Nature* **473**, 337–342 (2011).
28. T. S. Bayer, C. D. Smolke, Programmable ligand-controlled riboregulators of eukaryotic gene expression. *Nat. Biotechnol.* **23**, 337–343 (2005).
29. M. Tigges, T. T. Marquez-Lago, J. Stelling, M. Fussenegger, A tunable synthetic mammalian oscillator. *Nature* **457**, 309–312 (2009).
30. R. Haberman *et al.*, Therapeutic liabilities of in vivo viral vector tropism: Adeno-associated virus vectors, NMDAR1 antisense, and focal seizure sensitivity. *Mol. Ther.* **6**, 495–500 (2002).
31. B. C. Fuchs, J. C. Perez, J. E. Suetterlin, S. B. Chaudhry, B. P. Bode, Inducible antisense RNA targeting amino acid transporter ATB/OASCT2 elicits apoptosis in human hepatoma cells. *Am. J. Physiol. Gastrointest. Liver Physiol.* **286**, G467–G478 (2004).
32. P. Tebas *et al.*, Antiviral effects of autologous CD4 T cells genetically modified with a conditionally replicating lentiviral vector expressing long antisense to HIV. *Blood* **121**, 1524–1533 (2013).
33. M. Gossen, H. Bujard, Tight control of gene expression in mammalian cells by tetracycline-responsive promoters. *Proc. Natl. Acad. Sci. U.S.A.* **89**, 5547–5551 (1992).
34. H. K. Chung *et al.*, Tunable and reversible drug control of protein production via a self-excising degron. *Nat. Chem. Biol.* **11**, 713–720 (2015).
35. H. Saito *et al.*, Synthetic translational regulation by an L7Ae-kink-turn RNP switch. *Nat. Chem. Biol.* **6**, 71–78 (2010).
36. M. Filo, S. Kumar, M. Khammash, A hierarchy of biomolecular proportional-integral-derivative feedback controllers for robust perfect adaptation and dynamic performance. *Nat. Commun.* **13**, 2119 (2022).
37. M. Chevalier, M. Gómez-Schiavon, A. H. Ng, H. El-Samad, Design and analysis of a proportional-integral-derivative controller with biological molecules. *Cell Syst.* **9**, 338–353.e10 (2019).
38. Y. Qian, D. Del Vecchio, Realizing 'integral control' in living cells: How to overcome leaky integration due to dilution? *J. R. Soc. Interface* **15**, 20170902 (2018).
39. F. Ceroni, R. Algar, G. B. Stan, T. Ellis, Quantifying cellular capacity identifies gene expression designs with reduced burden. *Nat. Methods* **12**, 415–418 (2015).
40. T. Frei *et al.*, Characterization and mitigation of gene expression burden in mammalian cells. *Nat. Commun.* **11**, 4641 (2020).
41. R. D. Jones *et al.*, An endoribonuclease-based feedforward controller for decoupling resource-limited genetic modules in mammalian cells. *Nat. Commun.* **11**, 5690 (2020).
42. J. Nejepinska, R. Malik, S. Wagner, P. Svoboda, Reporters transiently transfected into mammalian cells are highly sensitive to translational repression induced by dsRNA expression. *PLoS One* **9**, e87517 (2014).
43. W. Ma, A. Trusina, H. El-Samad, W. A. Lim, C. Tang, Defining network topologies that can achieve biochemical adaptation. *Cell* **138**, 760–773 (2009).
44. R. P. Araujo, L. A. Liotta, The topological requirements for robust perfect adaptation in networks of any size. *Nat. Commun.* **9**, 1757 (2018).
45. M. H. Khammash, Perfect adaptation in biology. *Cell Syst.* **12**, 509–521 (2021).
46. D. Ausländer *et al.*, A synthetic multifunctional mammalian pH sensor and CO_2 transgene-control device. *Mol. Cell* **55**, 397–408 (2014).
47. C. D. Man *et al.*, The UVA/PADOVA type 1 diabetes simulator: New features. *J. Diabetes Sci. Technol.* **8**, 26–34 (2014).
48. C. Dalla Man, D. M. Raimondo, R. A. Rizza, C. Cobelli, GIM, simulation software of meal glucose–insulin model. *J. Diabetes Sci. Technol.* **1**, 323–330 (2007).

49. C. Dalla Man, R. A. Rizza, C. Cobelli, Meal simulation model of the glucose-insulin system. *IEEE Trans. Biomed. Eng.* **54**, 1740–1749 (2007).
50. B. P. Kovatchev, M. Breton, C. Dalla Man, C. Cobelli, In silico preclinical trials: A proof of concept in closed-loop control of type 1 diabetes. *J. Diabetes Sci. Technol.* **3**, 44–55 (2009).
51. Y. Zheng, S. H. Ley, F. B. Hu, Global aetiology and epidemiology of type 2 diabetes mellitus and its complications. *Nat. Rev. Endocrinol.* **14**, 88–98 (2018).
52. M. Stumvoll, B. J. Goldstein, T. W. van Haeften, Type 2 diabetes: Principles of pathogenesis and therapy. *Lancet* **365**, 1333–1346 (2005).
53. K. C. McCowen, A. Malhotra, B. R. Bistrian, Stress-induced hyperglycemia. *Crit. Care Clin.* **17**, 107–124 (2001).
54. G. Assessment; American Diabetes Association, 6. Glycemic targets: Standards of medical care in diabetes–2021. *Diabetes Care* **44**, S73–S84 (2021).
55. M. E. Lee, W. C. DeLoache, B. Cervantes, J. E. Dueber, A highly characterized yeast toolkit for modular, multipart assembly. *ACS Synth. Biol.* **4**, 975–986 (2015).
56. C. Engler, R. Kandzia, S. Marillonnet, A one pot, one step, precision cloning method with high throughput capability. *PLoS One* **3**, e3647 (2008).